LANDING SIMULATION OF A HIGH-ALTITUDE PLATFORM WITH SKID-TYPE LANDING GEAR – FLIGHT PROCEDURE, CONTROLLER, AND LOADS

Yasim J. Hasan[1], Nicolas Fezans[1] & Arne Voß[2]

[1]Institute of Flight Systems, German Aerospace Center (DLR), Lilienthalplatz 7, 38108 Braunschweig, Germany
[2]Institute of Aeroelasticity, German Aerospace Center (DLR), Bunsenstraße 10, 37073 Göttingen, Germany

Abstract

The German Aerospace Center (DLR) is currently developing a solar-powered high-altitude platform. The underlying vehicle is a fixed-wing aircraft designated to be stationed in the stratosphere for several days and to carry payload used to perform Earth observation missions. The project HAP addresses the complete design process of the aircraft, from conceptual studies and detailed design up to its construction, flight test campaigns and its final operational clearance. The aircraft operates at very low airspeeds, in the order of 10 m/s equivalent airspeed, and is therefore very susceptible to atmospheric disturbances, particularly in ground proximity. In addition, due to the absence of air brakes and due to the the very high glide ratio, the aircraft only reaches low sink rates, which additionally prolongates the landing duration. Altogether, the landing is a highly critical flight phase that needs thorough consideration. This paper addresses three issues associated with the landing: first, it presents a landing procedure that has a potential of reducing the risk of the landing, second, it describes the positioning process of skids that are used as landing gear, and third, it includes the resulting landing loads in the aeroelastic design. A high number of landing simulations of the aircraft in atmospheric disturbances is performed using a 6 degrees-of-freedom flight dynamics model. For this purpose, a landing controller based on an outer energy management loop and an inner pitch loop is implemented. During the simulations, the best main skid position is found to be around 40 cm in front of the centre of gravity. A dynamic aeroelasticity simulation is performed to analyse the associated loads. The results show that the landing loads obtained with this landing procedure are not sizing and thus do not influence the structural weight.

Keywords: High-Altitude Platform, Landing Simulations, Flight Control, Aeroelastic Sizing, Atmospheric Disturbances

Nomenclature

Abbreviations

CG	Centre of Gravity
DLR	Deutsches Zentrum für Luft- und Raumfahrt (German Aerospace Center)
HAP	High-Altitude Platform (name of a vehicle category and a DLR project)
HTP	Horizontal Tailplane
TECS	Total Energy Control System

Symbols

b	Wing, resp. horizontal tailplane, span
c_1, c_2	Stiffness constants
C_D, C_L, C_m	Drag, lift and pitching moment coefficients
d	Damping constant

e	Oswald efficiency factor
g	Gravitational acceleration at current location
h	Geodetic height
H	Transfer function
i_H	Horizontal stabiliser deflection
k_P, k_I, k_D	Controller gains
L_u, L_v, L_w	Longitudinal, lateral, and vertical turbulence scale lengths
M_x, M_z	Bending and torsional moments
m	Vehicle mass
$N_{Prop,LH\&RH}$	Propeller RPM left and right
q	Pitch rate
R_x, R_y, R_z	Skid forces in x, y and z-direction
t	Time
T	Thrust force
u, v, w	Velocity components in x, y and z-direction
$U_{flex,x}, U_{flex,z}$	Horizontal and vertical deflections
V_{TAS}	True airspeed
x, y, z	Cartesian coordinates
α	Angle of attack
ε	Downwash angle
γ	Flight path angle
Θ, Φ	Pitch and bank angles
Λ	Aspect ratio
μ, μ_S	Skid/ground longitudinal and lateral friction coefficients
σ	Standard deviation
$\sigma_1, \sigma_{1,HTP}, \sigma_2$	Parameters related to height above ground for ground effect model
τ	Time delay
τ_S	Skid crab angle

Indices

A	Aerodynamic value
AGL	Above Ground Level
b	Body-axis coordinate system
base	Baseline
c	Commanded value
EM	Value provided by energy management controller
g	Aircraft-carried normal earth axis system (North-East-Down)
GE	Ground effect
K	Flight path value
MG, TG, LWG, RWG	Main, tail, left wing and right wing gear
PC	Payload Compartment
TD	Touchdown
W	Wind value
WB	Wing-body

1. Introduction

High-altitude platforms (HAPs, *sg.* HAP) are air vehicles that operate at very high altitudes and can, if driven by solar power, stay airborne for weeks until landing becomes necessary again [1]. Therefore, HAPs are potential alternatives for typical satellite applications, including general Earth observation missions [2] and telecommunications [3]. For these applications, HAPs provide higher operational flexibility since they are not dependent on their orbit. Their lower altitude is advantageous in terms of image resolution and the level of disturbances due to the atmosphere. At the same time, one HAP

can only cover a limited area whereas one satellite can cover a much wider region of the Earth. In recent years, research on high-altitude platforms has increased sharply [4–8].

In the context of the project *HAP*, the German Aerospace Center (DLR) is developing a HAP system. The HAP system includes the fixed-wing HAP aircraft itself, the flight control system and the complete operational concept, the ground segment, the flight termination system and two instruments (payload) with a mass of up to 5 kg. The aircraft is designed to perform Earth observation missions carrying either a high-definition camera or a synthetic aperture radar. The aircraft development process is currently in the detail design phase. Within the further project term, the manufacturing, a comprehensive flight test campaign and a final high-altitude mission demonstration using the payload instruments will follow.

HAPs are designed to be stationed at high altitudes for a prolonged period of time. For fixed-wing aircraft this imposes the needs for a very high aerodynamic efficiency, a very low aircraft weight and a low airspeed. This, in turn, renders the landing one of the most challenging flight phases for HAPs. The very low airspeed in ground proximity makes the aircraft very susceptible to atmospheric disturbances. In addition, due to the need for a very low aircraft weight, air brakes are usually excluded. Together with the aircraft's high glide ratio, the achievable stable sink rates are low. As a consequence, the duration of the landing is prolongated, which increases the possibility of an encounter with gusts or wind shear. In addition, the successful execution of the landing in a designated area is vastly aggravated [9].

In case of the DLR HAP aircraft, there are two other factors that add to the complexity of the landing. First of all, with a total mass of around 140 kg, the aircraft is too heavy to be collected by hand and therefore needs a landing gear. However, a retractable gear would lead to an excessive weight penalty. Thus, small non-retractable skids are used as landing gear, which cause only little additional drag but bring some risks with respect to the landing, e.g. concerning high landing loads and rollovers. Furthermore, since there is not enough ground clearance, the propellers must be retracted before touchdown. From that moment on, a go-around cannot be initiated anymore.

These characteristics of the DLR HAP aircraft impose specific requirements on the way how final approach, flare, and landing can be performed. An easy-to-follow (i.e. which could potentially be flown manually) and robust landing procedure that accounts for the HAP's drawbacks and which is also applicable at slightly increased wind speeds is required. Furthermore, the skids need to be thoroughly dimensioned and positioned. Lastly, the resulting loads during the landing need to be examined and included in the aeroelastic design.

This paper addresses these landing issues by performing a high number of landing simulations of the aircraft in small atmospheric disturbances using a 6 degrees-of-freedom flight dynamics model. In order to apply appropriate commands in the simulations, an energy management control system is implemented and tuned in such a way that the required outer-loop commands could easily be provided by a human pilot if needed (reasonable control bandwidth and precision). Based on the results, the best skid positions are found and vertical velocities at touchdown are obtained that are used for a dynamic aeroelasticity simulation to analyse the associated loads. Section 2 presents the DLR HAP aircraft, section 3 briefly describes the mathematic models used for the calculations and section 4 outlines the landing controller. Subsequently, section 5 starts with a detailed presentation of the landing procedure defined. Furthermore, it shows the distribution of results for all landing simulations and documents the resulting skid positions. Finally, this paper shows the dynamic aeroelasticity simulation results in section 6 and closes with a conclusion in section 7 and a short outlook in section 8.

2. The DLR HAP aircraft

This section describes the DLR HAP aircraft. For this purpose, Figure 1 provides a schematic sketch of the vehicle. It has a wing area of around 40 m^2, a wing span of around 30 m and a total mass of aroung 140 kg. The wing is unswept and has dihedral tips with a dihedral angle of 12° while the inner

wing section has no dihedral angle. This version of the aircraft has ailerons[1] that are located rather close to the aircraft centreline. This position was chosen because, at larger spanwise positions, due to the high flexibility of the wing, torsional bending would lead to an aileron effectivity that would even be lower compared to the effectivity of the ailerons at the chosen position. Furthermore, a horizontal stabiliser, respectively an all-moving horizontal tail, is used for trimming and pitch control inputs. Yaw moments are realised by using a rudder. Detailed information on loads and aeroelastic analyses of the DLR HAP can be found in [10, 11] and insights into its flight mechanical design and analyses is provided by [12].
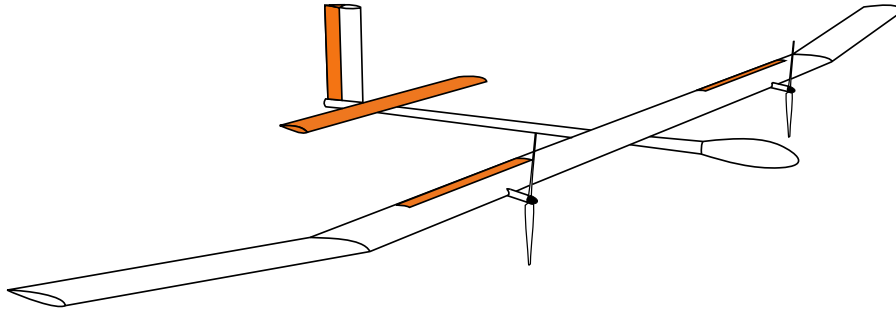

Figure 1 – Sketch of the DLR HAP aircraft with the control surfaces accentuated in orange colour

The HAP aircraft is equipped with four non-retractable rather soft skids that are used as landing gear (not shown in Figure 1). Here, three positions are defined a priori and are thus considered as fixed within this work. Those include the tail skid with a length of 0.1 m, being installed below the fuselage in the quarter line of the vertical tailplane and two wing skids, at the left and the right hand side, that are installed on the wing lower side at the kinks and in the wing quarter line. The wing skids' sizes are chosen such that they just have ground contact when the aircraft wing is in its jig shape. The main skid is installed below the fuselage and its chordwise position is varied within the works presented in this paper. In conformity with the nomenclature chosen in the flight dynamics model, the respective skids are denoted here with the indices MG (Main Gear), TG (Tail Gear), LWG (Left Wing Gear) and RWG (Right Wing Gear). Figure 2 illustrates the skid positions. It additionally shows the position of the lowest point of the payload compartment (PC), which is of significant importance in terms of finding the best main skid position.
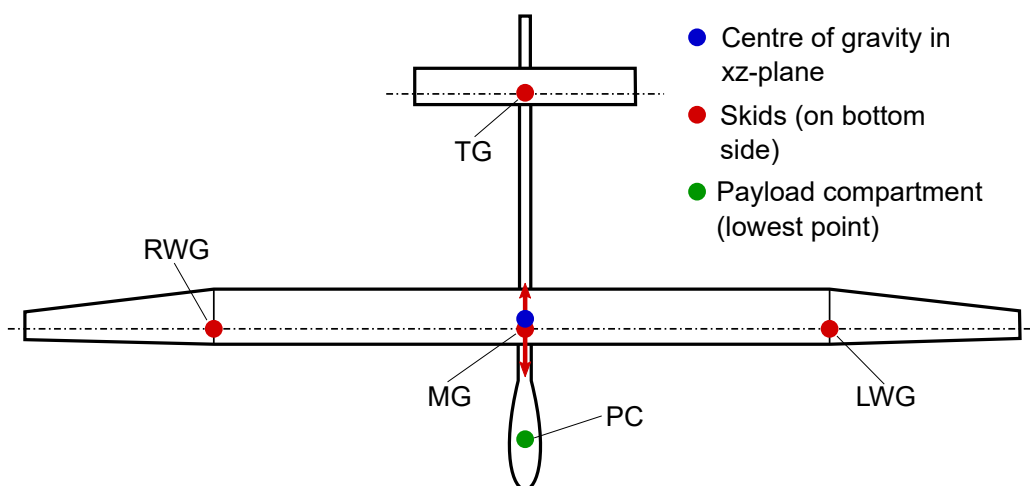

Figure 2 – Top view of HAP aircraft and skid positions

---

[1]Note that the current aircraft, which is intended to be investigated intensively during the flight test campaign, will be equipped with ailerons. For the final aircraft that it is intended to fly for several days at high altitudes, it is probable that the ailerons will be omitted.

While landing the HAP aircraft, it is crucial that the main skid touches down first. It should be noted that tail dragger aircraft usually touch down with the rear gear first in order to land with a higher angle of attack. In addition, the probability of a liftoff is lower since the angle of attack further decreases while lowering the main gear. However, in case of HAP, such a procedure is not possible. This is due to the fact that a first contact on one of the other skids could easily overstress the extremely lightweight structure and even seriously damage it. This circumstance adds to the fact that landing the HAP aircraft is a comparatively difficult task. Similarly, the payload compartment, storing the highly sensitive payload instruments, must never make ground contact either. Hence, it is possible to define an allowable pitch range at touchdown (TD) that must be kept to ensure that the aircraft is not damaged. Figure 3 shows a schematic sketch of the way the minimum and maximum allowable pitch angles are defined. The pitch range is exaggerated in the picture, for readability reasons, but is very narrow in practice and lies, depending on the main skid size and position, between around $-3°$ and $+1°$.
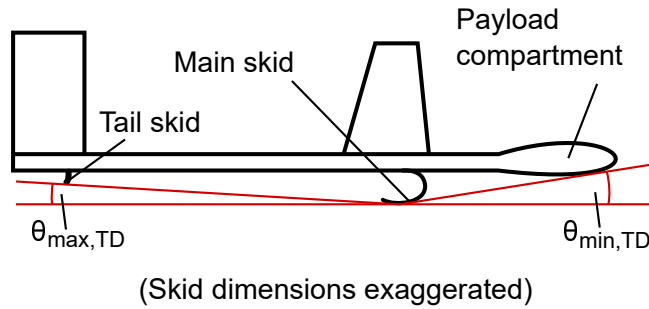

(Skid dimensions exaggerated)

Figure 3 – Side view of HAP aircraft and approximate allowable pitch angles at touchdown

Lastly, the HAP aircraft is equipped with two propeller engines with a diameter of 1.7 m. It is obvious that there is not enough ground clearance for the propellers to rotate below about 0.85 m height over ground. Therefore, the propellers need to be retracted at some point during the landing process.

3. Flight Dynamics Model Formulation

The flight dynamics model used within this work is a six-degrees-of-freedom model with a derivative-based aerodynamic model and a quasistatic dynamic pressure-dependent approach to account for flexibility effects due to the flight shape. Note that a model including the structural dynamics is currently under development and will be used for later works. In the context of this approach, different sets of aerodynamic derivatives are provided for different flight shapes and, thus, for different equivalent airspeeds. For intermediate airspeeds, linear interpolation is performed. More information on the flight dynamics model used here can be found in [9].

3.1 Ground Effect Model

The flight dynamics model used within this work contains a ground effect model (GE) that is based upon the approach proposed in [13–15]. At this time, solely the ground effect for the longitudinal motion is respected. In the modelling approach the following ground impact factors are defined for wing-body (WB) and the horizontal tailplane (HTP):

$$\sigma_1 = 1 - \tanh\left(a_1 \cdot \frac{h_{WB_{AGL}}}{b}\right)$$

$$\sigma_{1,HTP} = 1 - \tanh\left(a_1 \cdot \frac{h_{HTP_{AGL}}}{b_{HTP}}\right)$$

$$\sigma_2 = 1 - \tanh\left(a_2 \cdot \frac{h_{WB_{AGL}}}{b}\right)$$

(1)

Herein, a_1 and a_2 are modelling coefficients and b is the wing span. The quantities $h_{WB_{AGL}}$ and $h_{HTP_{AGL}}$ represent the altitude above ground of the wing neutral point, respectively the HTP neutral point. The

effects on the wing-body and the HTP lift coefficients are modelled as

$$C_{L_{WB}} = C_{L_{WB,base}} + C_{L\alpha_{WB,GE}} \cdot \sigma_1 \cdot \alpha$$
$$C_{L_{HTP}} = C_{L_{HTP,base}} + C_{L\alpha_{HTP,GE}} \cdot \sigma_{1,HTP} \cdot \alpha_{HTP},$$

(2)

where $C_{L\alpha_{WB,GE}}$ and $C_{L\alpha_{HTP,GE}}$ are the associated ground effect modelling terms. The ground effect impact on the drag coefficient can be expressed by a decrease in induced drag:

$$C_D = C_{D_{base}} - \sigma_1 \cdot \frac{C_L^2}{e\Lambda\pi}$$

(3)

The attenuation of main wing downwash is given by

$$\varepsilon_{HTP} = \varepsilon_{HTP_{base}} + \left(\frac{\partial \varepsilon_{HTP}}{\partial \alpha}\right)_{GE} \cdot \sigma_2 \cdot \alpha \left(t - \tau\right).$$

(4)

Finally, the zero pitching moment changes due to the presence of the ground. The influence is modelled by using a simple offset:

$$C_m = C_{m_{base}} + \sigma_1 \cdot C_{m0_{GE}}$$

(5)

The underlying aerodynamic data were provided by the aerodynamics specialist of the *HAP* flight physics team. For their generation, the vortex lattice method *Athena Vortex Lattice* (AVL), developed at MIT [16, 17] was used. Therein, the ground presence was modelled using the mirror principle, signifying that the aircraft and thereby its associated circulation distribution was mirrored below the ground. The provided aerodynamic information was then introduced into the flight dynamics model by fitting the parameters presented above to these data.

3.2 Skid Model

This section briefly outlines the approach used to model the landing gear forces and, correspondingly, the resulting moments. As already described, skids are used as landing gear for the HAP aircraft. The aircraft is equipped with a main skid, two skids at the left and right hand sides of the main wing and a tail skid. For all skids, the same viscoelastic properties, hence stiffness and damping are assumed. A control point is defined on the lower side of the payload compartment to monitor whether ground contact occurred or not. Whenever this is the case, the respective landing is deemed unacceptable. The skids are modelled with standard linear solids (SLS) as described in Figure 4. The skid reference point is geometrically defined as the lowest point of the skid, i.e. the point at which the skid would touch the ground assuming no longitudinal or lateral inclination and a perfectly flat ground surface. The dynamic equations of such spring-damper systems can be found in numerous publications, see for instance in [18]. The associated vertical force is either zero whenever there is no ground contact or dependent on the compression and vertical velocity of the respective skid. For all skids the vertical forces are given by

$$\dot{R}_{z,g_{Skid}} = \begin{cases} \dot{h}_{AGL_{Skid}} \cdot c_1 + h_{AGL_{Skid}} \frac{c_1 \cdot c_2}{d} - R_{z,g_{Skid}} \frac{c_1 + c_2}{d} & : h_{AGL_{Skid}} < 0 \text{ m} \\ 0 & : h_{AGL_{Skid}} \geq 0 \text{ m}. \end{cases}$$

$$R_{z,g_{Skid}} = \begin{cases} \int \dot{R}_{z,g_{Skid}} \, dt & : h_{AGL_{Skid}} < 0 \text{ m} \\ 0 & : h_{AGL_{Skid}} \geq 0 \text{ m}. \end{cases}$$

(6)

Herein, $h_{AGL_{Skid}}$ is the altitude above ground of the skid reference point of the respective skid. It includes the effect of the elastic deformation of the aircraft. For the spring constants c_1 and c_2 a value of $40\,000$ N/m is used, which was proposed by the aeroelasticity specialist of the flight physics team. This value represents very soft skids that are supposed to reduce the loads at touchdown. For the damper constant, a value of 500 Ns/m is used, which was adjusted manually, such that a seemingly realistic touchdown behaviour is obtained. Together with the longitudinal and lateral friction forces all resulting forces in body-fixed coordinates are given by

$$R_{x,b_{Skid}} = \mu \cdot \text{sign}(u_{K,b_{Skid}})R_{z,g_{Skid}}\cos\left(\Theta\right) - R_{z,g_{Skid}}\sin\left(\Theta\right)$$
$$R_{y,b_{Skid}} = \mu \cdot \text{sign}(u_{K,b_{Skid}})R_{z,g_{Skid}}\sin\left(\Phi\right)\sin\left(\Theta\right) - \mu_S \cdot \text{sign}(\tau_S)R_{z,g_{Skid}}\cos\left(\Phi\right) + R_{z,g_{Skid}}\sin\left(\Phi\right)\cos\left(\Theta\right)$$
$$R_{z,b_{Skid}} = \mu \cdot \text{sign}(u_{K,b_{Skid}})R_{z,g_{Skid}}\cos\left(\Phi\right)\sin\left(\Theta\right) + \mu_S \cdot \text{sign}(\tau_S)R_{z,g_{Skid}}\sin\left(\Phi\right) + R_{z,g_{Skid}}\cos\left(\Phi\right)\cos\left(\Theta\right),$$
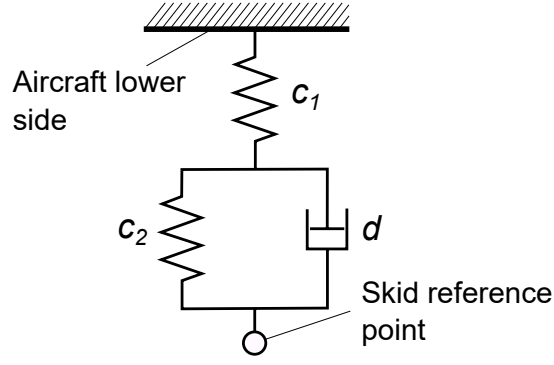
(7)

Figure 4 – Skid modelled as standard linear solid in Kelvin-Voigt representation

where τ_S is the skid crab angle. It is assumed that it is the same for all skids. It reads

$$\tau_S = -\arctan\left(\frac{v_{K,b_{Skid}}}{u_{K,b_{Skid}}}\right). \tag{8}$$

For the kinetic friction coefficient, a value of $\mu = 0.4$ is used, derived as an average value from measurements for metal skids on a dry lakebed [19–21]. For the lateral kinetic friction coefficient a somewhat higher value of $\mu_S = 0.55$ is assumed. Note that this is a very simplified approach to account for the form of the skids, which have better slide properties in longitudinal direction than in lateral direction. Since in the landing simulations performed in this work the lateral direction only plays a minor role, this modelling approach is deemed sufficient. However, for later simulations that also involve touchdowns with crab angles, the skid model will be further revised. In addition, the main skid model contains a standstill logic that assures a force equilibrium as soon as the aircraft comes to a standstill.

3.3 Turbulence Model

In the context of this work, continuous turbulence is applied to the aircraft within the simulations. The respective wind speeds are modeled for the translational wind components by passing white noise through a filter. The respective forming filters are such that approximate von Kármán velocity spectra are obtained [22]. The corresponding transfer functions read

$$H_u(s) = \frac{\sigma_u\sqrt{\frac{L_u}{V_{TAS}}}\left(1 + 0.25\frac{L_u}{V_{TAS}}s\right)}{1 + 1.357\frac{L_u}{V_{TAS}}s + 0.1987\left(\frac{L_u}{V_{TAS}}\right)^2 s^2}$$

$$H_v(s) = \frac{\sigma_v\sqrt{\frac{L_v}{V_{TAS}}}\left(1 + 2.7478\frac{L_v}{V_{TAS}}s + 0.3398\left(\frac{L_v}{V_{TAS}}\right)^2 s^2\right)}{1 + 2.9958\frac{L_v}{V_{TAS}}s + 1.9754\left(\frac{L_v}{V_{TAS}}\right)^2 s^2 + 0.1539\left(\frac{L_v}{V_{TAS}}\right)^3 s^3} \tag{9}$$

$$H_w(s) = \frac{\sigma_w\sqrt{\frac{L_w}{V_{TAS}}}\left(1 + 2.7478\frac{L_w}{V_{TAS}}s + 0.3398\left(\frac{L_w}{V_{TAS}}\right)^2 s^2\right)}{1 + 2.9958\frac{L_w}{V_{TAS}}s + 1.9754\left(\frac{L_w}{V_{TAS}}\right)^2 s^2 + 0.1539\left(\frac{L_w}{V_{TAS}}\right)^3 s^3}$$

where σ_u, σ_v and σ_w are the standard deviations of the wind velocity for the longitudinal, lateral, and vertical axes and L_u, L_v and L_w the corresponding scale lengths. The associated values are derived from the boundary layer turbulence data of [23]. The values for an altitude of 10 m are used and assumed constant in the range between 0 m and 10 m. To account for the fact that the HAP aircraft is supposed to land only when the degree of turbulence is comparatively low, the values in [23] are divided by a factor 2. Table 1 documents the resulting values.

It should be noted that the approach to model the turbulence intensity and the scale lengths as proposed in CS-AWO [24] was considered but it did not seem to yield realistic turbulence parameters

Table 1 – Standard deviations and scale lengths used within this work to model turbulence

Altitude range	σ_u (m/s)	σ_v (m/s)	σ_w (m/s)	L_u (m)	L_v (m)	L_w (m)
$h < 10$ m	1.155	0.835	0.575	21	11	5

when flying very close to the ground (< 1 m). With decreasing height above ground, a sharp increase in turbulence level is specified and seems quite unrealistic for turbulence in close ground proximity in otherwise fairly low-turbulence and low-wind conditions.

4. Landing Controller

In the context of this work, numerous landing simulations are performed in the form of batch calculations. Therefore, a landing controller that realises appropriate control inputs within these simulations is needed. However, for reasons of weight reduction, the HAP aircraft will not be equipped with a radar altimeter. Hence, no information about the altitude over ground is available and, accordingly, the HAP aircraft is supposed to be piloted manually during landing. Thus, the controller performance needs to apply inputs that can also be applied by a pilot rather than to provide the best possible control characteristics. Generally, it needs to

- apply rather lower frequency control inputs,

- apply rather simple commands, and

- rely on flight parameters that are available to or directly observable by the pilot during manual landing. These include e.g., the airspeed and the pitch angle via telemetry and the height above ground through observation on the airfield.

The landing controller consists of two nested loops. The outer loop manages the energy and is strongly inspired by the well-known total energy control system (TECS) philosophy [25, 26]. Whilst the overarching idea of TECS remained, the inner-working has been significantly modified to achieve a better performance. The modifications of the TECS control concept will be published separately in the near future. For the purpose of the present work and the analysis of the results, the energy management outer loop can be thought as a very well-performing TECS controller. The energy management outer loop is combined with a simple inner pitch loop and an inverse thrust model converting thrust commands into propeller rotation speed command. Figure 5 shows the block diagram of the complete control system used for the landing.

As will be seen in more detail in section 5 the major purpose of the controller used here is to help designing a procedure that reduces the general risk of damaging the vehicle during landing, e.g., through hard landing, ground contact of the payload compartment or an initial touchdown of any skid other than the main skid. For this purpose, the landing is subdivided into different phases. Therefore, the control system includes a phase manager that consists of a state machine and provides the current phase in output such that the control functions can know the current phase of the landing procedure and behave accordingly. The phases of the landing are (confer also the more detailed descriptions of these phases in section 5):

$$Phase = \begin{cases} 0 & : \ t < t_{Start} \\ 1 & : \ t \geq t_{Start} \\ 2 & : \ |h_{AGL} - h_{\text{``Flare''}}| \leq \Delta h_{max} \quad \text{consecutively for duration } t_h \\ 3 & : \ |\Theta - \Theta_{Target,TD}| \leq \Delta\Theta_{max} \quad \text{consecutively for duration } t_\Theta \end{cases} \tag{10}$$

The simulation is initialised in stabilised horizontal flight at 10 m above ground and the control function in phase 0 maintains this condition. Upon reaching $t = t_{Start}$, phase 1 is activated and the initial descent to the altitude $h_{\text{``Flare''}}$ is initiated. As soon as this altitude is reached and the aircraft maintains to stay within the band of $\pm\Delta h_{max}$ for the duration of t_h consecutively, the autoland controller switches to
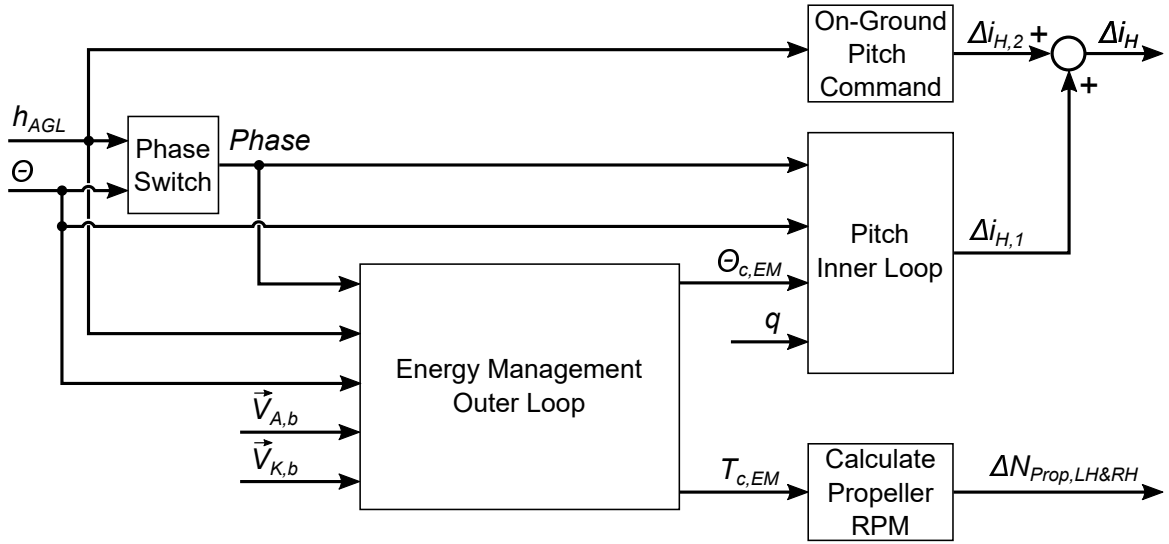
Figure 5 – Block diagram of the landing controller

phase 2. In this phase the aircraft needs to capture the pitch angle $\Theta_{Target,TD}$. Finally, after having kept the pitch angle at $\Theta_{Target,TD}$ for a couple of seconds, phase 3 is activated, which consists in shutting off the engines and retracting the propellers and the final descent until touchdown while keeping $\Theta = \Theta_{Target,TD}$. This also signifies that the aircraft does not perform a flare in a typical sense. Instead, airspeed is decreased at the altitude that is here called $h_{"Flare"}$ and the aircraft then sinks until touchdown. Such a procedure is chosen since a typical flare is not feasible with the HAP aircraft. Nevertheless, as will be shown in section 5, the associated sink rates at touchdown are low.

The pitch inner loop tracks the pitch angle command $\Theta_{c,EM}$ from by the energy management controller by means of a PID controller, which commands the stabiliser deflection $\Delta i_{H,1}$:

$$\Delta i_{H,1} = k_{P,\Theta} \cdot (\Theta_c - \Theta) + k_{I,\Theta} \left(\frac{\omega_\Theta^2}{s^2 + 2\zeta_\Theta \omega_\Theta + \omega_\Theta^2} \Theta_c - \Theta \right) + k_{P,q} \cdot q \tag{11}$$

For the integral element, a second-order filter is applied to the pitch command signal Θ_c. This can be interpreted as a kind of reference model and allows to prevent the integral element from causing overshoot in the response to pitch command changes. The controller parameters $k_{P,\Theta}$, $k_{I,\Theta}$ and $k_{P,q}$ are manually adjusted. Depending on the respective phase, the pitch command signal is either the output of the energy management loop or the (constant) touchdown target pitch angle:

$$\Theta_c = \begin{cases} \Theta_{c,EM} & : \ Phase = 1 \\ \Theta_{Target,TD} & : \ Phase = [2,3] \end{cases} \tag{12}$$

After touchdown a soft pitch up is commanded to ensure that the tail skid makes ground contact soon after touchdown. The resulting stabiliser input is generated as a single integral element, which is applied as an offset to the stabiliser deflection angle at touchdown to realise a smooth transition:

$$\Delta i_{H,2} = \begin{cases} i_{H,TD} - k_{I,\Theta,oG} \int dt & : \ \text{any skid on ground} \\ 0 & : \ \text{otherwise} \end{cases} \tag{13}$$

The parameter $k_{I,\Theta,oG}$ is defined such that, ideally, neither a liftoff nor a touchdown of the payload compartment occurs. Before the initiation of phase 3, the thrust command $T_{c,EM}$ is translated into a propeller RPM input. After the initiation of phase 3, the engines are shut off and $T_{c,EM}$ is not used anymore.

5. Landing Simulations

This section presents the results of the landing simulations with the flight dynamics model using the landing controller presented above. The general procedure that has been sketched already when presenting the controller is detailed in section 5.1. Subsequently, it presents the skid positioning process based on batch landing simulations.

5.1 Landing Procedure

As already described, there are a couple of factors that make landing the DLR HAP aircraft a challenging task with a relativity high risk of damaging the vehicle. The most important contributing factors are:

- High susceptibility to atmospheric disturbances

- Very low sink rate

- Skids as landing gear

- Pitch angle demand to remain with a very narrow range for touchdown

- Necessity to retract propellers before touchdown and therefore no option for go-around anymore shortly after retraction

In order to cope with these challenges, a landing procedure has been developed that subdivides the landing process in different phases. The controller from section 4 is set up to follow the reference inputs within these stages and all landings of the batch simulations presented in the following section are performed this way.

Figure 6 shows the evolution of the main flight parameters during this landing procedure for a simulation with von Kármán turbulence. The different phases are depicted in the plot in the fifth row on the left hand side labelled "Controller Phase". In the beginning, the signal is zero, signifying that the controller is not active, respectively that landing has not yet been initiated. After 5 seconds, the final descent starts and during the complete landing process, all phases are run through. They are:

1. **Phase 1 - Descent and capture of $h_{"Flare"}$:** The landing starts by a descent up to a predefined altitude over ground, which is here called $h_{"Flare"}$, even though, strictly speaking, the aircraft does not perform a flare in a typical sense. The altitude $h_{"Flare"}$ is signalised by the green dashed line in Figure 6 (first column, second row). It needs to be chosen as near to the ground as possible but should offer enough ground clearance that both the engines can still be used and a light gust does not directly lead to ground contact of any part of the aircraft. The altitude $h_{"Flare"}$ needs to be maintained for a couple of seconds before the transition to phase 2 is realised.

2. **Phase 2 - Deceleration while maintaining $h_{"Flare"}$ and capture of safe pitch attitude Θ_{Target}:** The main skid needs to touch down first. However, together with the small skid size, the allowable pitch band at touchdown is very narrow (confer Figure 2). The fourth plot on the left hand side, showing the pitch angle Θ, illustrates this. It shows the minimum allowable pitch angle $\Theta_{min,TD}$ at touchdown (bottom horizontal dashed red line), limited by the payload compartment, and the maximum allowable pitch angle $\Theta_{max,TD}$ at touchdown (top horizontal dashed red line), limited by the tail skid. In addition, a target pitch angle Θ_{Target} is defined that lies in this band but is closer to the maximum allowable pitch angle, since this is the softer limit. This target pitch angle is also the angle that should be held during touchdown. In this phase, the altitude $h_{"Flare"}$ is maintained while the aircraft decelerates. In doing so, the angle of attack increases along with the pitch angle, while the flight path angle is zero. As soon as the target pitch angle Θ_{Target} is reached, the flight is stabilised and continued for a couple of seconds.

3. **Phase 3 - Depletion of remaining kinetic and potential energy while keeping safe pitch attitude** Θ_{Target}**:** This phase is initiated by shutting the engines off, retracting the propellers and locking them in a position parallel to the wing leading edge before approaching the ground. Since Θ_{Target} must be held and the aircraft can no longer generate thrust, no real control of the sink rate is possible anymore. The airspeed decreases and the aircraft starts to sink, which to some extent alleviates the sink rate. The remaining kinetic and potential energies decrease simultaneously. This maneuver can only be performed safely if the pitch angle constraints (due to the skid geometry) and the propeller radius permit to initiate this phase at a sufficiently low altitude over ground and to use a Θ_{Target} that is large enough to prevent too high sink rates. The design of this vehicle allows this. This phase is critical in terms of gusts or system faults as no go-around manoeuvre can be initiated anymore. As soon as the main skid touches down, the stabiliser is slightly pulled to ensure that the payload compartment does not make ground contact.

4. **Pitch up during slideout:** This final step of the landing procedure is not considered a distinct phase, but it is crucial to land the aircraft safely. After touchdown, the controller commands a pitch up that reduces the risk that the payload compartment makes ground contact. The pitch up needs to be sufficiently soft in order to prevent the aircraft to become airborne again or to induce too high loads on the tail skid.

As shown in Figure 6, the landing is completed successfully in this case. The main skid is the first skid to touch down, as shown by the plot for the normalised skid force $R_{z,MG}/m$ (sixth plot on the right hand side). The moment of the first contact between any part of the aircraft and the ground is marked by a vertical dotted line. A couple of seconds after touchdown, the tail skid makes ground contact ($R_{z,TG}/m$). As intended, the associated tail skid force is very low and does not introduce heavy loads into the structure. As the wing deflection due to flexibility decreases along with the airspeed while being on ground, and thereby with the wing unloading, the left ($R_{z,LWG}/m$) and right wing ($R_{z,RWG}/m$) skids touch down. As requested, the payload compartment never makes ground contact. In this case, the main skid was located 0.4 m forward of the aircraft centre of gravity (CG), but one of the motivations for building this simulation program and scenario is to optimise the positions of the main skid. An interesting fact is that the main skid force at touchdown is lower than the maximum force, which occurs right before the wing skids touch down. This signifies that due to the very low sink rate, the landing shock is relatively low. Instead, the weight plays the major role in terms of the maximum skid force. As soon as the airspeed decreases while being on ground, lift decreases and the skid force increases to a higher level compared to the shock at touchdown.

5.2 Skid Positioning

In order to find an appropriate position for the main skid and make sure that this choice is robust against variations of the system parameters and atmospheric conditions, a large number of landing simulations are performed in batch. The main input parameters are the atmospheric conditions, in particular stochastic turbulence. The main output parameters are the skid forces and the ground clearance at the payload compartment. The simulation program also provides the vertical speeds at touchdown that are used for the aeroelastic loads analysis presented in section 6. Four scenarios are considered for the main skid position, see Table 2.

Table 2 – Main skid positions with respect to the aircraft CG investigated in this study. Note that a positive value signifies a location forward of the CG.

Main skid positions			
+0.0 m	+0.2 m	+0.4 m	+0.6 m

For each main skid position, 1000 simulations are performed. Within the simulations, the HAP aircraft is subject to light atmospheric disturbances such as it is assumed to be acceptable for the landing of
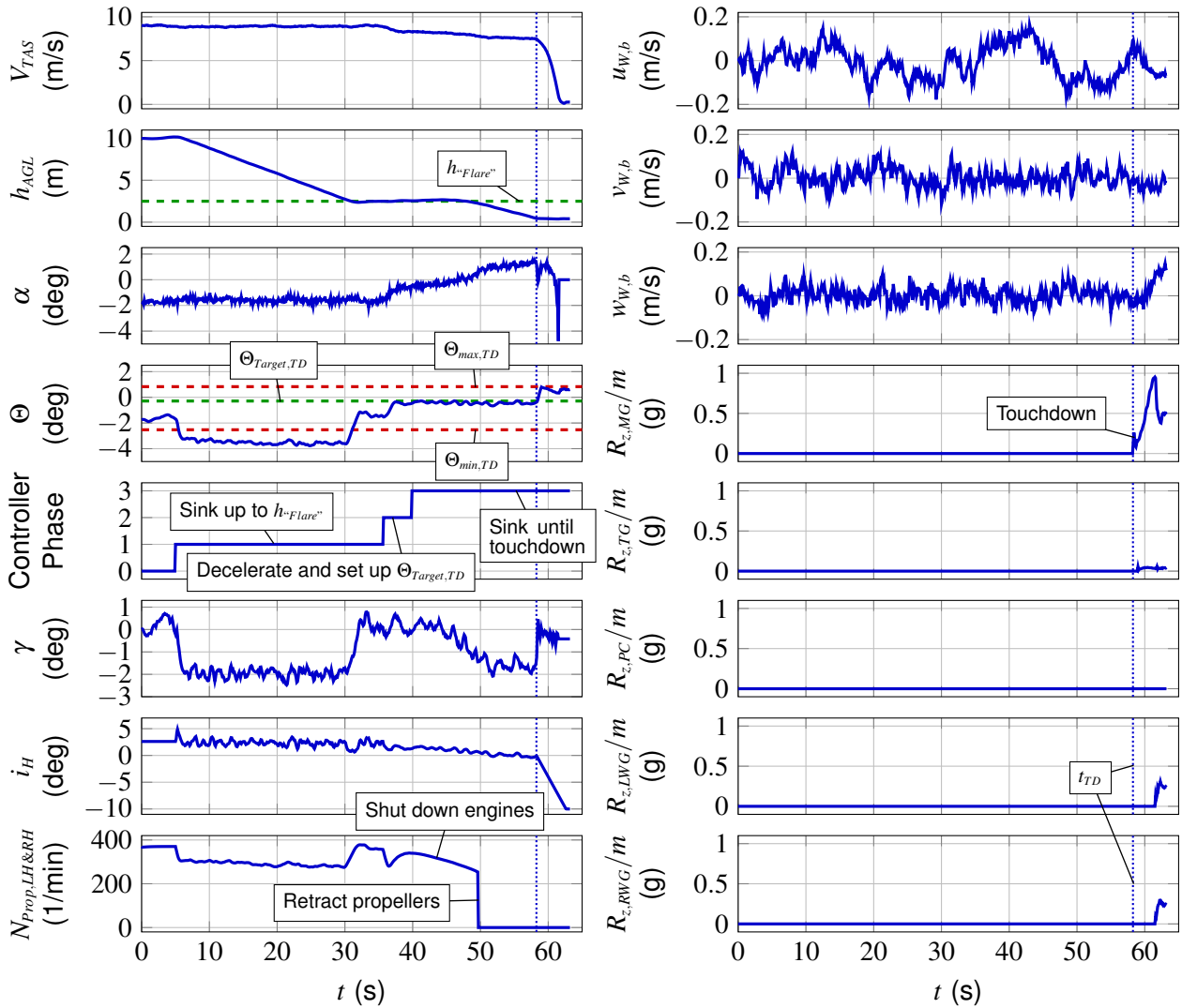
Figure 6 – Procedure proposed for landing, shown for an exemplary landing with the landing skids 0.4 m forward of the CG

this aircraft. The disturbances are modelled according to section 3.3 and applied to all three axes. Within these simulations, the underlying white noise seeds needed for the turbulence generation are varied, leading to differences in the wind velocities between the runs. The variations are performed independently for all three axes and at random. The landing controller presented in section 4 is used for each simulation. Hence, every landing is performed using the procedure shown in Figure 6.

Figure 7 shows some selected results of these batch simulations in form of box plots. In all plots, the inner horizontal bar represents the median of the distributions. The box itself is defined by the upper and lower quartiles and the whiskers are here defined by the 2%-percentile, resp. the 98%-percentile. This signifies that 25% of the data points are located inside the box above the median and 25% of the data points are in the box below the median. Analogously, 23% of the distribution is located below the box and above the lower whisker, and 23% are above the box and below the upper whisker. The remaining 4% of the data points are explicitly plotted as blued points.

On the left hand side, the minimum altitude above ground that occurred during the simulation for the respective skid is illustrated for the main skid ($h_{AGL,MG_{min}}$), the tail skid ($h_{AGL,TG_{min}}$) and the payload compartment ($h_{AGL,PC_{min}}$). Here, a negative altitude signifies a compression of the respective skid. Hence, in this case, there has been ground contact of this skid during the simulation. In contrast, if the value is positive, the respective skid has not touched down. The right hand side shows the normalised vertical skid forces due to skid compression and damping for the same skids.
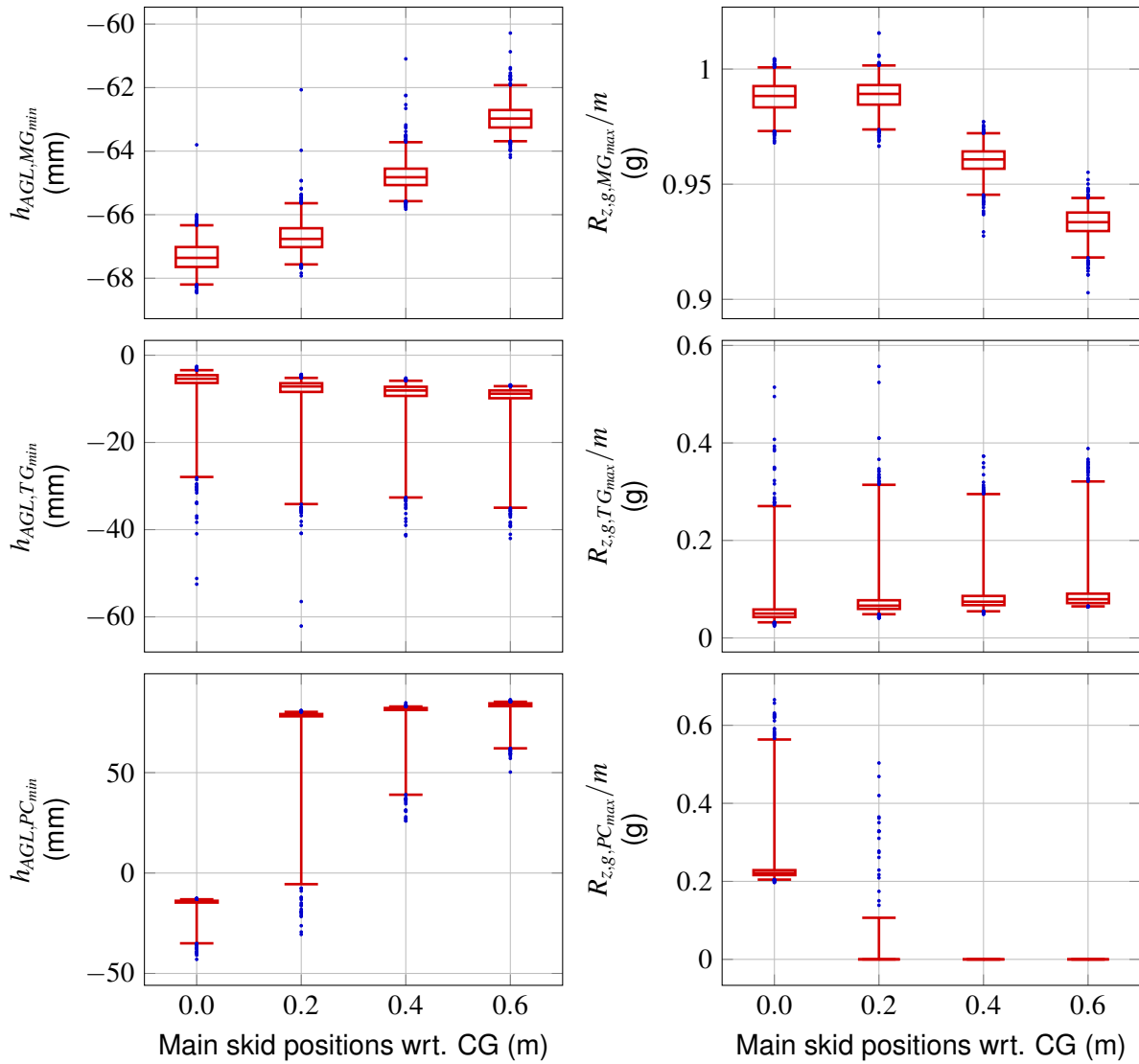
12

Figure 7 – Box plots for minimum altitude over ground and maximum normalised vertical skid forces that occurred during the landing simulations for different main skid positions and for main skid, tail skid and payload compartment. For each different skid position, 1000 landing simulations were performed.

As illustrated by the plots in the first row, an increase of the main skid position leads to a decrease of the same skid's maximum compression, resp. minimum altitude. This is also accompanied by a decrease of the maximum vertical skid forces. As shown in section 5.1, the maximum main skid force rather results from the aircraft weight than from the landing shock. The more forward the main skid is located, the earlier the tail gear touches down, sharing a part of the aircraft weight. This is due to the fact that the pitching moment due to the main skid landing force, causing the aircraft to pitch up, increases with a forward shift of this skid. Accordingly, the maximum main skid forces slighty decrease.

Consequently, the tail skid loads (plots in the second row) slightly increase along with the main skid position. It is also observable that the tail skid forces have a much stronger variation compared to the main skid forces. While the main skid force is mainly dependent on the aircraft sink rate, the tail skid force tends to be rather driven by the pitching motion at and after touchdown. As a consequence, a slight variation of the aircraft attitude and rotational motion at the moment of touchdown has a much larger impact on the tail skid movement.

Finally, the third row shows that the main skid position has a major influence on whether the payload compartment touches the ground or not. For a main skid location directly at the x-position of the

CG, the payload compartment always makes ground contact, which is logical as the friction force causes the aircraft to pitch down and this rotation is then stopped by the contact force between the ground and the payload compartment. For a main skid position of 0.2 m ahead of CG, landings without ground contact as well as landings with ground contact, in some cases with high associated loads on the payload compartment, were obtained. For the two front-most positions of 0.4 m or 0.6 m, the payload compartment never makes ground contact. It must however be noted that, with around $50\ mm$, the clearance is still small for these cases. However, due to the aircraft geometry and the limited main skid height, much more payload clearance is not achievable. If a larger clearance at the payload compartment was desired, then a higher main skid would be required. Both 0.4 m or 0.6 m positions are appropriate for the main skid. Based on the simulation results, it can also be concluded that the defined procedure is adequate for landing this aircraft in light turbulence.

At the end, as a compromise, the main skid has been placed 0.4 m forward of the CG. While this position is sufficient to maintain a relatively low probability of ground contact of the payload compartment, this position is, on average, associated with slightly lower tail skid forces than the position at 0.6 m. In addition, the closer the main skid position is located to the CG, the lower the fuselage bending moment at touchdown becomes.

The analyses presented in this section are based on the skid model presented in section 3.2. While for the inflight dynamics, the accuracy of the given model can be assumed to be sufficient for a "flight mechanical" landing simulation, the structural dynamics at touchdown should be analysed with more sophisticated models. Therefore, the landing loads are investigated in more detail in section 6. In this analysis, the aircraft is placed midair right above the ground with a prescribed sink rate and the simulation is run. In order to determine an appropriate sink rate for the aeroelasticity analyses, the results of the batch simulations are used. Figure 8 shows the distribution of the sink rate of the main skid at the moment of touchdown over the respective normalised main skid forces (one point per simulation).
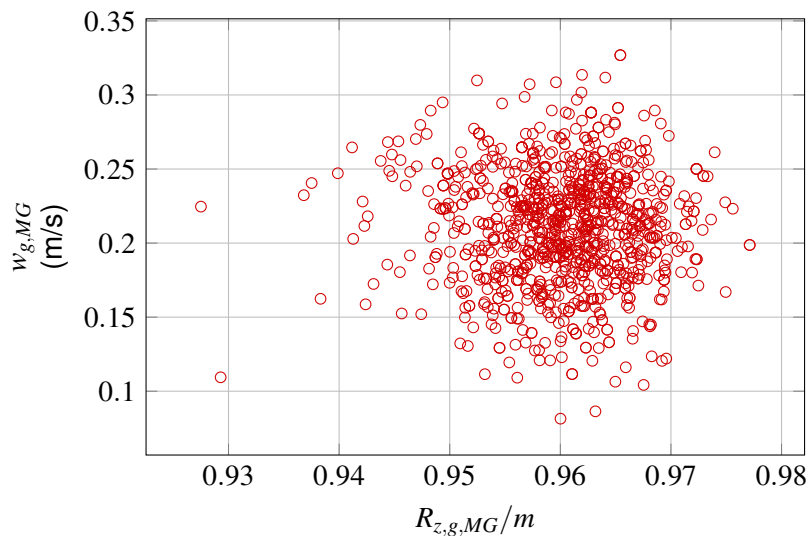

Figure 8 – Distribution of vertical speed at the moment of touchdown over the normalised vertical skid force for the main skid and for the main skid position at 0.4 m forward of the CG. 1000 landing simulations were performed.

As shown, the main skid sink rates are spread over a range of 0.05 m/s to 0.33 m/s. It is observable that there is no correlation between sink rate and vertical skid force. This again makes clear that the landing shock is not the driver for the maximum forces. The variation instead results from variations of the aircraft behaviour on ground due to differences in attitude and rotational rates at touchdown. It can be concluded that a soft landing of the HAP aircraft is usually performed with sink rates of 0.35 m/s or lower. The hard landing case is defined by multiplying this upper-bound on the sink

rate by 2, i.e., by a sink rate of 0.7 m/s. These sink rate values are used for the loads calculations presented in the following section.

6. Aeroelastic Loads

During the loads analysis of the HAP configuration [11], which is performed by the DLR Institute of Aeroelasticity, multiple load cases are considered, including 1260 maneuver loads, 2016 "1-cos" gust encounters, 54 engine loads, and 4 landing load cases. The highest resulting section loads are used for the sizing of the primary aircraft structure, e.g., for the wing typical quantities these are the bending moment M_x and the torsional moment M_y. Thus, it would be beneficial if the landing loads stay within the load envelope and don't drive the sizing and/or the aircraft design significantly.

For the calculation of the landing loads, aeroelastic models are used, which include mass, structural and aerodynamic models. An overview of the models is given in Figure 9 and more details can be found in [10, 27]. Some important differences with respect to the flight-mechanical modelling are that the mass model consists of multiple discrete masses, which allows to calculate inertial forces. The aerodynamic model is based on a vortex lattice method [28], which provides discrete distributed forces and moments, too. This is an essential prerequisite to obtain section loads. The structural dynamic response of the aircraft is captured using a modal approach in combination with a modal truncation. The landing skids are modeled in a similar way as described in section 3.2. Because the vertical forces from the landing impact are considered most important for the loads analyses, the model is simplified in such a way that it includes only forces R_x in x and R_z in z-direction, the aircraft pitch angle is small and is neglected and, in a conservative approach, the damping is set to zero. During the time domain simulations, the forces from the landing skids are applied to the structural model and the elastic structural deflection of the attachment nodes are communicated back to the landing skid model, which is important when calculating the height above ground h_{AGL}.

The aeroelastic time domain simulations start with the trimmed aircraft at a given sink rate (0.35 to 0.7 m/s, compare with section 6) just a few centimeters above ground and with a simulated time of 3.0 to 5.0 seconds (until the aircraft stops). Note that because the aircraft is trimmed at a given sink rate, modelling the ground effect is not necessary and because the simulation starts just before touch down, no landing controller is necessary.

Figure 10 shows the height above ground h_{AGL} and the vertical forces R_z of the four landing skids during a landing simulation at a sink rate of 0.7 m/s (hard landing case). At the beginning of the simulation, the aircraft is at a constant sink rate and at ≈ 0.2 s, the main landing skid touches the ground. The height above ground h_{AGL} of the main landing skid becomes negative, indicating an elastic compression, and a vertical force R_z occurs immediately and with a peak at ≈ 0.3 s. Next, the tail skid touches the ground at ≈ 2.0 s and with much lower forces R_z. As the aircraft slows down, the aerodynamic lift decreases and the wing deflection slowly decreases until the left and right wing landing skids touch the ground at ≈ 3.0 s. Towards the end of the simulation, the aircraft has nearly stopped and it can be seen that with $R_{z,MG} \approx 1100$ N, most of the aircraft mass is supported by the main landing skid. It is interesting to see that the peak of the landing impact at ≈ 0.3 s is actually lower than the final value, which can be explained by the high structural flexibility of the aircraft. The minimal and maximal flexible structural deflections $U_{flex,x}$ in x and $U_{flex,z}$ in z-direction of the wings are shown in Figure 11. Next to the large change of the wing bending $U_{flex,z}$ during the landing simulation, it can be seen that the sudden deceleration of the aircraft also causes an in-plane motion of the wings with $U_{flex,x} = -7.0$ to $+2.0$ cm at the wing tips.

During the preliminary design and with higher, more conservative sink rates, the landing impact actually had an influence on the highest bending moments M_x in the outer wing. The more detailed knowledge of the landing phase obtained in this work resulted in lower sink rates so that the landing load cases are now within the envelopes from maneuver and gust loads and no longer influence the structural sizing.

7. Conclusion

The aim of this paper was to investigate three issues associated with the landing of the DLR HAP aircraft, being the general landing procedure, the positioning of the landing skids and the inclusion of the landing loads in the aeroelastic design. For this purpose, the paper briefly presented the HAP

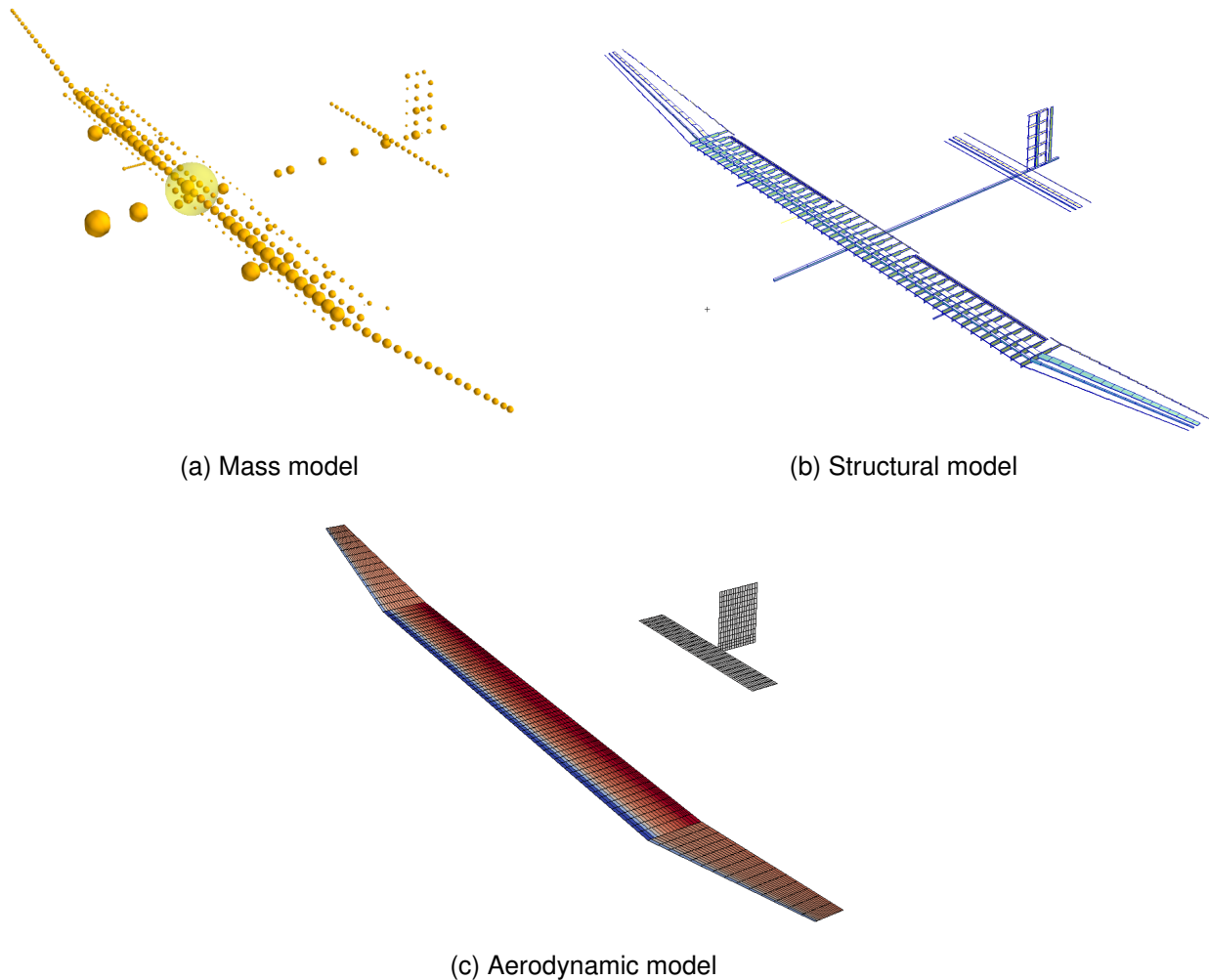(a) Mass model

(b) Structural model

(c) Aerodynamic model

Figure 9 – Mass, structural, and aerodynamic models

aircraft and gave an insight into the modelling of the ground effect and the skid model within the flight dynamics model used in this work.

Furthermore, the paper presented a flight controller used to automatise the landing. Since the HAP aircraft is supposed to be landed manually, the aim of the flight control design was not to implement an appropriate and robust controller for real flight. Rather, a controller that generates inputs that a pilot can also apply needed to be designed, which could be used for the successive batch analysis. The controller realises a landing procedure based on three phases from initial descent over a deceleration at a constant altitude up to shutting down the engines and a final descent until touchdown. The controller is based upon an energy management approach and a simple PID pitch inner loop.

Subsequently, the paper dealt with the landing analysis. First, a single landing in turbulence using the afore-defined controller was investigated in more detail and the respective phases were explained. Second, batch analyses were performed for four different main skid positions. In doing so, the turbulence was varied at random and independently for all three axes and 1000 simulations were performed for every skid position variation. It could be shown that the main skid forces decrease along with moving the main skid forward, which can be attributed to the geometry-driven target pitch angle at touchdown. Furthermore, the average tail skid loads slightly increase along with a forward shift of the main skid position. For main skid positions of 0.4 m and 0.6 m forward of the centre of gravity, the aircraft payload compartment did not make ground contact in any of the simulations, which was a major requirement. Therefore, the procedure proved to be adequate for landing the HAP aircraft. However, even though the flight controller applied rather simple and lower frequency commands, it is yet to be investigated whether a pilot can perform a landing following this procedure similarly well.
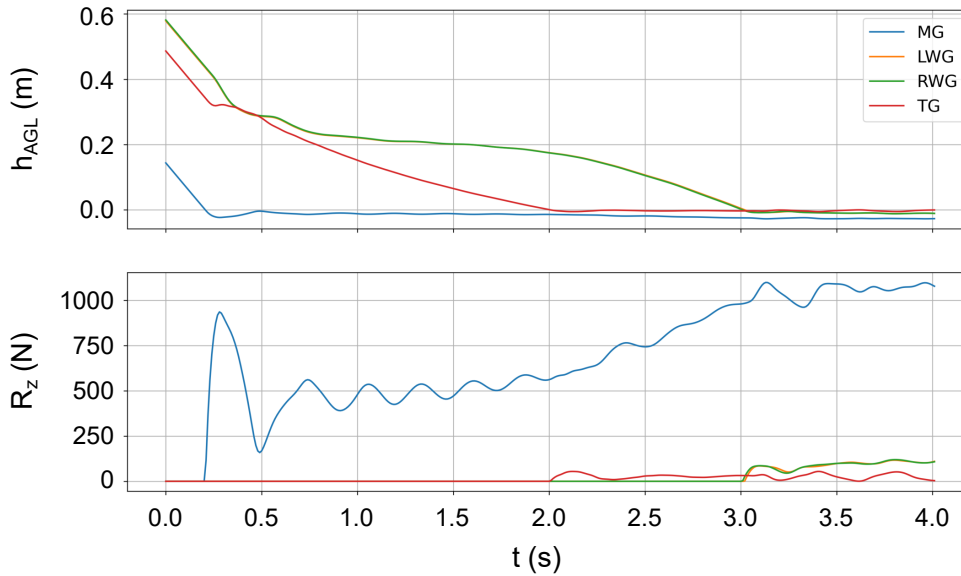
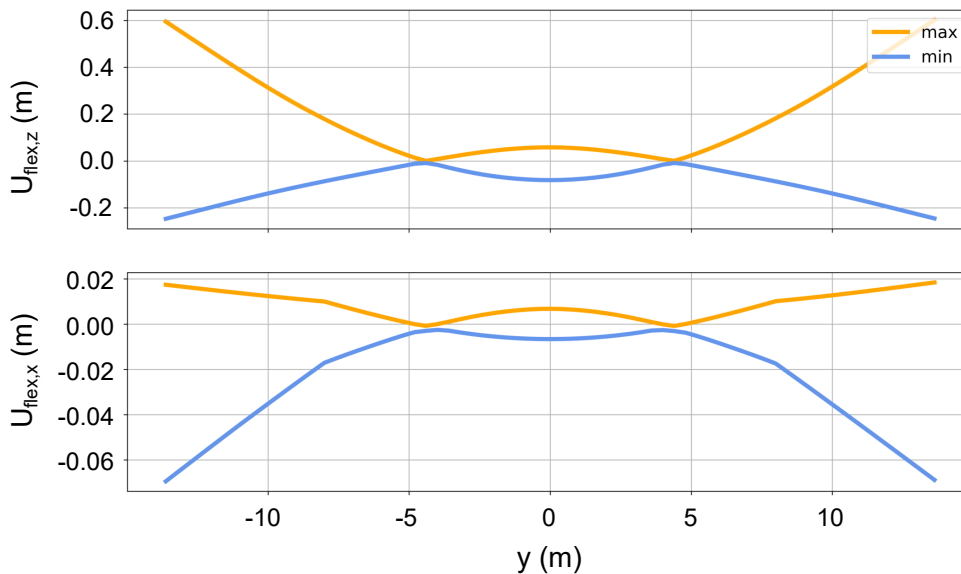Figure 10 – Landing skid positions h_{AGL} and vertical forces R_z

Figure 11 – Elastic wing deflections in vertical ($U_{flex,z}$) and horizontal ($U_{flex,x}$) direction

Finally, a sink rate of 0.35 m/s for a soft landing and 0.7 m/s for a hard landing were selected based on the batch simulation results for the subsequent dynamic aeroelastic analysis.

It should be noted that the skid force calculation was based on a standard linear solid model and the frictions coefficients were simply assumed to be constant. In addition, the ground was assumed to be flat. Therefore, it can be assumed that the simulation of the final slideout is less realistic. Furthermore, no ground effect influence on the lateral motion dynamics was modelled. Hence, the impact of the lateral wind was less representative. However, the main aim of this analysis was to investigate the landing until touchdown with a special focus on the question which skid makes ground contact first. This question is mainly driven by the longitudinal motion and by the vertical skid forces rather than by the friction forces. Hence, it can be assumed that the modelling approach used here is sufficiently accurate and, thus, the results are significant.

Finally, a dynamic aeroelasticity calculation was performed in order to include the landing loads in the loads analysis and the associated structural sizing. In doing so, the aircraft was placed midair a couple of centimetres above ground with the prescribed sink rates for a soft and a hard landing and simulations over touchdown and until standstill were undertaken. It turned out that, even for the hard landing, the associated loads are within the envelopes from maneuver and gust loads and therefore do not influence the structural sizing.

8. Future Work

In the landings dealt with in this paper, rather low atmospheric turbulence was applied. With the resulting main skid position every landing could be completed successfully. However, another important question that will be investigated in future works is, up to which degree of turbulence, safe landings can still be performed with this landing procedure. Furthermore, it needs to be examined, whether a pilot is able to apply input commands that are equivalent to those applied by the landing controller in order to follow the landing procedure and how much training would be necessary to achieve a high landing success rate. For this purpose, a desktop simulation session with pilots will be performed in future works.

Acknowledgements

Contact Author Email Address

yasim.hasan@dlr.de

Copyright Statement

References

[1] Airbus Defence and Space, *Airbus Zephyr, Solar High Altitude Pseudo-Satellite flies for longer than any other aircraft during its successful maiden flight*, Press Release, 8th August 2018. [Online]. Available: https://www.airbus.com/newsroom/press-releases/en/2018/08/Airbus-Zephyr-Solar-High-Altitude-Pseudo-Satellite-flies-for-longer-than-any-other-aircraft.html.

[2] Runge, H., Rack, W., Ruiz-Leon, A., and Hepperle, M., "A Solar Powered HALE-UAV for Arctic Research," in *1st CEAS European Air and Space Conference*, Berlin, Germany, September 2007.

[3] Mohammed, A., Mehmood, A., Pavlidou, F.-N., and Mohorcic, M., "The Role of High-Altitude Platforms (HAPs) in the Global Wireless Connectivity," in *Proceedings of the IEEE*, vol. 99, November 2011, pp. 1939–1953. DOI: 10.1109/JPROC.2011.2159690.

[4] National Aeronautics and Space Administration, Dryden Flight Research Center, *Solar-Powered Research and Dryden*, NASA Facts: FS-1998-10-0054 DFRC, available online at https://www.nasa.gov/centers/dryden/pdf/120308main_FS-054-DFRC.pdf, 1998.

[5] D'Oliveira, F., Melo, F., and Devezas, T., "High-altitude platforms - present situation and technology trends," in *Journal of Aerospace Technology and Management*, vol. 8, Aug. 2016, pp. 249–262. DOI: 10.5028/jatm.v8i3.699.

[6] Ross, H., "Fly around the World with a Solar Powered Airplane, AIAA-2008-8954," in *The 26th Congress of International Council of the Aeronautical Sciences (ICAS), Anchorage, Alaska*, 14.-19. September 2008. DOI: 10.2514/6.2008-8954.

[7] Nunez, C., "Solar Impulse 2 Completes Trip Around World, Demonstrates Clean Energy and Aviation," *National Geographic*, 25th July 2016, Available online at https://www.nationalgeographic.com/news/2016/07/solar-impulse-completes-trip-around-world-abu-dhabi-solar-power-airplane/.

[8] Stevens, P., "Zephyr: Pioneering the Stratosphere, zp-pn-0039v2.0," in *Exploring an Unmanned Future Conference*, Presentation, available online at https://aaus.org.au/wp-content/uploads/2019/03/Paul-Stevens-Airbus-at-AAUS-Exploring-an-Unmanned-Future-Conference-20190225.pdf, Melbourne and Avalon: Australian Association for Unmanned Systems, 25th February 2019.

[9] Hasan, Y. J., Roeser, M. S., and Voigt, A. E., "Evaluation of the Controllability of a High-Altitude Platform in Atmospheric Disturbances Based on Pilot-in-theLoop Siulations," *Deutscher Luft und Raumfahrtkongress, Bremen and online*, August - September 2021.

[10] Voß, A., Handojo, V., Weiser, C., and Niemann, S., "Preparation of Loads and Aeroelastic Analyses of a High Altitude, Long Endurance, Solar Electric Aircraft," in *AEC2020 Aerospace Europe Conference*, Bordeaux, France, 2020.

[11] Voß, A., Handojo, V., Weiser, C., and Niemann, S., "Results from Loads and Aeroelastic Analyses of a High Altitude, Long Endurance, Solar Electric Aircraft," in *Journal of Aeroelasticity and Structural Dynamics*, vol. 9, Department of Aerospace Engineering of Politecnico di Milano, January 2022. DOI: 10.3293/asdj.2021.58.

[12] Hasan, Y. J., Roeser, M. S., Hepperle, M., Niemann, S., Voß, A., Handojo, V., and Weiser, C., "Flight Mechanical Design and Analysis of a Solar-Powered High-Altitude Platform," *Deutscher Luft und Raumfahrtkongress, online*, September 2020.

[13] Fischenberg, D., "Identifizierung des Bodeneffektes und der Fahrwerksaerodynamik des ATTAS aus Flugversuchsdaten (in English: Identification of the Ground Effect and the Landing Gear Aerodynamics of the ATTAS Based on Flight Test Data)," DLR Institute of Flight Mechanics, Tech. Rep. DLR-IB 111-94/22, 1994.

[14] Fischenberg, D., "Ground Effect Modeling Using a Hybrid Approach of Inverse Simulation and System Identification," in *A Collection of the AIAA Modeling and Simulation Technologies Conference Technical Papers*, Portland, Oregon, 1999, pp. 427–434.

[15] Jategaonkar, R. V., *Flight Vehicle System Identification - A Time Domain Merthodology: Second Edition*, ser. Progress in Astronautics and Aeronautics. Reston, VA, USA: AIAA, 2015, vol. 245, ISBN: 978-1-62410-278-3.

[16] Drela, M., *Flight Vehicle Aerodynamics*, The MIT Press, 2014.

[17] Drela, M. and Youngren, H., *AVL User Primer*, Available online at https://web.mit.edu/drela/Public/web/avl/.

[18] Argatov, I. I., "Mathematical modeling of linear viscoelastic impact: Application to drop impact testing of articular cartilage," in *The International Conference on BioTribology 2011*, July 2013, pp. 213–225.

[19] McKay, J. M. and Scott, B. J., *Landing-gear Behavior During Touchdown and Runout for 17 Landings of the X-15 Research Airplane*, ser. NASA TM X-518. National Aeronautics and Space Administration, 1961.

[20] Wilson, R. J., *Drag and wear characteristics of various skid materials on dissimilar lakebed surfaces during the slideout of the X-15 airplane*, ser. NASA TN D-3331. National Aeronautics and Space Administration, 1966.

[21] Sefic, W. J., *Friction Characteristic of Steel Skids Equipped with Skegs on a Lakebed Surface*, ser. NASA TM 81347. National Aeronautics and Space Administration, 1979.

[22] Gage, S., "Creating a Unified Graphical Wind Turbulence Model from Multiple Specifications, AIAA 2003-5529," in *AIAA Modeling and Simulation Technologies Conference and Exhibit, Austin, Texas, USA*, August 2003. DOI: https://doi.org/10.2514/6.2003-5529.

[23] Johnson, D. L. and Vaughan, W. W., *NASA/TM-2008-215633, Terrestrial Environment (Climatic) Criteria Guidelines for Use in Aerospace Vehicle Development, 2008 Revision*. National Aeronautics and Space Administration, Marshall Space Flight Center, Alabama, December 2008.

[24] European Aviation Safety Agency, *Easy Access Rules for All Weather Operations (CS-AWO)*, February 2018.

[25] Lambregts, A. A., "Vertical flight path and speed control autopilot design using total energy principles, AIAA paper 83-2239," in *Guidance and Control Conference, Gatlinburg, Tennessee, USA*, Aug. 1983, pp. 559–569. DOI: https://doi.org/10.2514/6.1983-2239.

[26] Lambregts, A. A., "Integrated system design for flight and propulsion control using total energy principles, AIAA paper 83-2561," in *Aircraft Design, Systems and Technology Meeting, Fort Worth, Texas, USA*, Oct. 1983. DOI: https://doi.org/10.2514/6.1983-2561.

[27] Voß, A., Koch, C., Niemann, S., Handojo, V., and Weiser, C., "Transition from Preliminary to Detailed Design of a Highly Elastic Solar Electric Aircraft," in *International Forum on Aeroelasticity and Structural Dynamics*, to be published, Madrid, Spain, 2022.

[28] Voß, A., "An Implementation of the Vortex Lattice and the Doublet Lattice Method," DLR Institute of Aeroelasticity, Göttingen, Germany, Technical Report DLR-IB-AE-GO-2020-137, October 2020. [Online]. Available: https://elib.dlr.de/136536/.